JOURNAL OF AIRCRAFT
Vol. 52, No. 5, September–October 2015

Assessment of Noise Level Variations of Aircraft Flyovers Using Acoustic Arrays

Dick G. Simons,* Mirjam Snellen,† and Bert van Midden‡
Delft University of Technology, 2629 HS Delft, The Netherlands
and
M. Arntzen‡ and D. H. T. Bergmans§
National Aerospace Laboratory/NLR, 1059 CM Amsterdam, The Netherlands

DOI: 10.2514/1.C033020

Variability in noise levels for flyovers of the same aircraft type can be as large as 12 dB, hampering noise assessment around airports. The variable atmosphere (affecting the acoustic propagation) and variations in the aircraft emitted noise are considered as the two main contributors to the noise level variability. This paper presents two experiments aimed at quantifying these contributions. First, the atmospheric contribution was determined with a loudspeaker (100 m height) sending signals to microphones on the ground, indicating a sound level variability of less than 2 dB. Second, noise levels from Boeing 737 flyovers (landings) were measured with an acoustic camera. The observed noise level variability was 6–8 dB. The acoustic camera imaging capabilities eliminated variations due to ground reflections and ambient noise, and identified the turbofan engines as the dominant noise source. Assuming the two contributions to be independent statistical processes, with the atmosphere contributing 2 dB maximally, it is concluded that the total noise level variability (6–8 dB) as measured for the flyovers was entirely due to the source. Correlating the engine noise levels to the fan rotational speed (from the spectrograms) shows that variations in engine setting explain over 70% of the observed total noise level variation.

Downloaded by TU DELFT on February 15, 2018 | http://arc.aiaa.org | DOI: 10.2514/1.C033020

I. Introduction

IN THE Netherlands, but also in many other countries, the noise levels used for the planning and monitoring of aviation are based on calculations. The majority of the models used for the calculations rely on the so-called noise–power–distance (NPD) tables [1–6]. These provide noise levels at predefined distances for a large number of aircraft and flight procedures. The NPD data are based on information provided by the aircraft manufacturers and are gathered, for example, during certification. The use of NPD data in model predictions results in approximate and averaged, but fixed, values of the actual aircraft noise levels. In addition, NPD data account for atmospheric conditions only in an average sense.

Therefore, prediction of the noise levels for a certain aircraft type, flight phase, and location will show no variability and provide a unique noise level only. In reality, however, measurements taken during flyovers of a specific aircraft type do show a significant variation. These variations are known to be the results of changes in atmospheric propagation conditions (including variations in the ground interaction), varying aircraft configurations (e.g., engine, aerodynamic devices, and landing gear settings) and contributions of other interfering noise sources. Variations as large as 12 dB can be observed directly under the flight path, as can be seen in Fig. 1 [7], even when corrected for differences in the aircraft position and aircraft attitude relative to the receiver.

These noise level variations, observed for the same aircraft types, are problematic for noise assessment around airports and the related enforcement of environmental laws, since the noise levels used for enforcement can deviate significantly from the real levels, resulting either in too many aircraft movements within the set limits or in unused capacity.

In the presented research, we aim to obtain the fundamental insights required to solve this issue. To this end, we will focus on the individual contributions of the main causes for the variability, i.e., the effect of the atmosphere on the acoustic propagation and variations in the emitted noise at the source (i.e., the aircraft).

For assessing the variations in noise levels resulting from the varying atmosphere, a dedicated experiment has been carried out. This experiment is extensively described in the literature [7] and briefly repeated here in Sec. II.A. The final results and conclusions (i.e., the maximum contribution of atmospheric effects to the variation in received noise levels) are also reported in Sec. II.A.

To assess the total variability in received noise levels due to variations in the noise levels emitted by the aircraft, measurements of the noise of aircraft flyovers have been carried out with an acoustic camera. In this way, the effects of the ground reflection and ambient noise are largely eliminated. In addition, the availability of measurements with microphone arrays allows for assessing the contribution of the individual aircraft noise sources to the total noise level. The acoustic camera used contains 32 microphones in a spiral configuration. The measurements were carried out for a series of flyovers at Rotterdam–The Hague Airport for a single aircraft type, i.e., the Boeing 737-700 (all from the same airline). Section II.B describes the acoustic camera measurements at the airport, whereas Sec. III presents the analysis of these array measurements. A full assessment of the measured variability is given in Sec. IV and, finally, conclusions are drawn in Sec. V.

The objective of this paper is to quantify the contributions of both the varying atmosphere as well as variations in emitted noise levels to the variations in the received noise levels in the aircraft landing phase.

II. Experimental Setup

A. Cabauw Measurements and Analysis

At the meteorological tower of the Royal Netherlands Meteorological Institute (KNMI) at Cabauw, a loudspeaker was positioned 100 m above the ground; see Fig. 2. The loudspeaker was programmed to emit a 15-s-long white noise signal of 100 dB every

Received 6 June 2014; revision received 2 April 2015; accepted for publication 22 May 2015; published online 9 September 2015. Copyright © 2015 by Delft University of Technology. Published by the American Institute of Aeronautics and Astronautics, Inc., with permission. Copies of this paper may be made for personal or internal use, on condition that the copier pay the $10.00 per-copy fee to the Copyright Clearance Center, Inc., 222 Rosewood Drive, Danvers, MA 01923; include the code 1533-3868/15 and $10.00 in correspondence with the CCC.

*Full Professor, Aircraft Noise and Climate Effects, Faculty of Aerospace Engineering, Kluyverweg 1.
†Associate Professor, Aircraft Noise and Climate Effects, Faculty of Aerospace Engineering, Kluyverweg 1.
‡Ph.D. Student, Aircraft Noise and Climate Effects, Faculty of Aerospace Engineering, Kluyverweg 1.
§Research and Development Engineer, Environment and Policy Support, Anthony Fokkerweg 2.

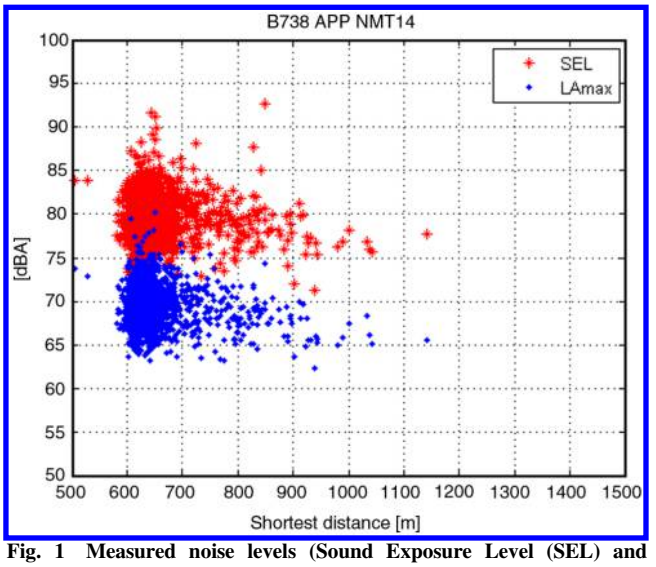

Fig. 1 Measured noise levels (Sound Exposure Level (SEL) and maximum A-weighted level (LAmax)) directly under the flight path during approach (APP) [7].

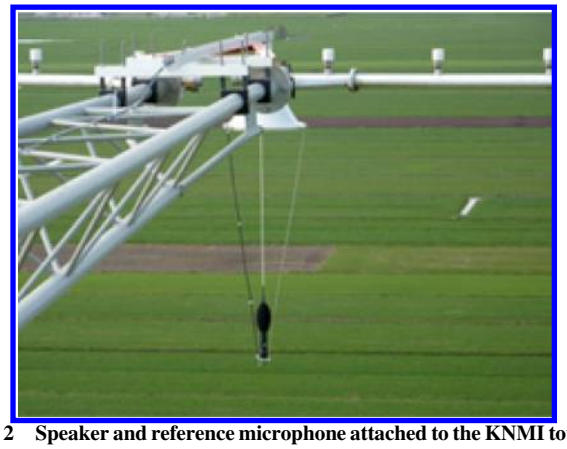

Fig. 2 Speaker and reference microphone attached to the KNMI tower.

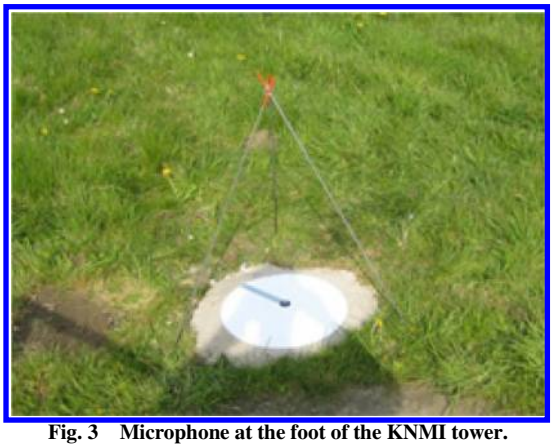

Fig. 3 Microphone at the foot of the KNMI tower.

hour, except during the night time to prevent excessive noise levels in the surrounding area. The signal bandwidth was 250 Hz–4 kHz.

This signal was recorded by a microphone directly in front of the loudspeaker, as well as by five microphones positioned on the ground. The microphone sampling frequency was 48 kHz. The 1/3 octave band levels were determined according to [8]. These microphones were mounted flush on a 40 cm metal plate. One of these five microphones can be seen in Fig. 3. The microphones on the ground measured the signal with full ground reflection. To obtain free-field conditions, the theoretical 6 dB were subtracted from the recorded signal.

Due to the characteristics of the loudspeaker, the emitted audio signal did not fully match the signal fed into the speaker. Therefore, the transmission loss between the source and the microphones on the ground was calculated using the measurements of the microphone in front of the speaker as the source signal.

In addition to the acoustic measurements, various weather parameters were also measured during the experiment, including wind velocity, wind direction, ambient temperature, and humidity. Many of these parameters were measured at multiple heights. Hence, exact knowledge regarding the weather conditions during each sound event was available.

The overall measurement period ranged over more than one year [9], which allowed searching for correlations between the acoustic data and the weather data for weather conditions encountered during a full year.

The transmission loss was analyzed for different frequency bands in the range from 500 to 3000 Hz only. Below 500 Hz, the signal-to-noise ratio (SNR) deteriorated due to the presence of background noise. Due to the vicinity of neighboring communities and speaker characteristics, the maximum sound level at the source was limited. Consequently, for emitted sound with a frequency above 3000 Hz, atmospheric absorption caused the SNR to also deteriorate.

To obtain a clear impression of the wind and turbulence effects, the influence of atmospheric absorption on transmission loss was removed [10]. Due to the varying humidity and temperature, the absorption coefficient varied between the data points. In addition, the spherical spreading term was removed as well, which reduced the acoustic data to so-called excess transmission loss, i.e., the loss in sound level that was not due to absorption and geometrical spreading.

Using simple one-dimensional linear regression analysis and multivariate regression analysis, correlations were searched between excess transmission loss (for the various frequency bands) and the corresponding weather parameters. The multivariate analysis [11] allowed for determining the combined influence of the atmospheric variables on excess transmission loss.

Some results of this correlation analysis can be found in the literature [9] but, actually, no statistically significant correlations between the acoustic variables and weather variables were found. However, from analysis of the complete dataset, the total variability observed in excess transmission loss amounted to ~2 dB [7,9]. Figure 4 presents an example of measured excess transmission loss at 1000 Hz for microphone 2.

Now, the microphone array measurements at the airport (see Sec. II.B) were taken during landing when the aircraft passed at approximately 40 m altitude, i.e., more than a factor of two less than the 100 m source-receiver distance at the Cabauw measurements.

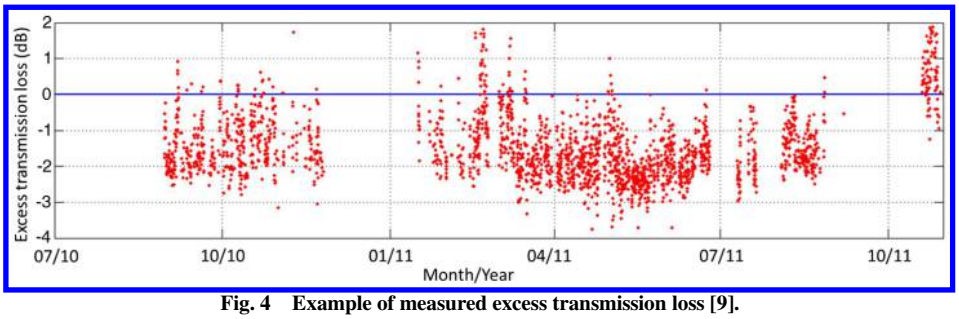

Fig. 4 Example of measured excess transmission loss [9].

Downloaded by TU DELFT on February 15, 2018 | http://arc.aiaa.org | DOI: 10.2514/1.C033020

Downloaded by TU DELFT on February 15, 2018 | http://arc.aiaa.org | DOI: 10.2514/1.C033020

According to literature, there is a linear relation between excess attenuation and height for heights below 100 m (see figure 2 of [12]). Hence, we assume the total variability in excess transmission loss due to meteorological variations at a 40 m altitude (the conditions of the flyover measurements at the airport) to be less than that at a 100 m altitude, which is in accordance with [13], indicating high agreement in the noise levels of repetitive flyovers where the aircraft flew at constant settings. We further assume this conclusion to also hold for the frequency band of the flyover measurements described here.

It should be remarked that the total noise level variability observed for the aircraft landings is 6–8 dB (see Sec. IV). Assuming the variability due to the atmosphere and the source (i.e., the aircraft) to be independent statistical processes, it can be concluded that variability due to the source is dominant.

B. Acoustic Array Measurements

Measured in number of passengers, Rotterdam–The Hague Airport is The Netherlands's third largest airport, coming after Schiphol Airport and Eindhoven Airport. Typically, each day, 5 to 10 Boeing 737 aircraft land at the airport. For the measurements, the acoustic camera was positioned as close as possible to, and in line with, the airport runway, as illustrated in Fig. 5. Figure 6 shows the acoustic camera setup.

The acoustic camera used for the flyover measurements consisted of 32 microphones. The distribution of the microphones over the array was flexible and could be selected random, along circles, crosses, or spirals [14–18]. This distribution determines the resolution and the presence of side and grating lobes, indicating acoustic sources at locations with no sound source present. For the array measurements presented in this contribution, a spiral configuration was selected; see Fig. 7. The diameter of the array was 2 m. The microphones were mounted in a wooden plate that was covered with foam, to at least partially eliminate reflections. Filters in the data acquisition system cut off frequencies below 45 Hz and above 11,200 Hz. The data acquisition system operated at a sample frequency of 100 kHz. The sound was not recorded continuously but was split into blocks of 20 ms, giving 2000 samples per block. Furthermore, gaps of 40 ms existed between the sound blocks to allow for storing the data.

In total, 20 flyovers were measured, of which eight were selected for further analysis. These were acquired in October and November of 2011 and in April and May of 2012. Measurements were carried out during the daytime and for days with low windspeeds. Temperatures ranged from 10 to 20°C. All eight flyovers corresponded to the same aircraft type (i.e., the Boeing 737-700) equipped with the same engine type (CFM56-7B22). Information about the flight was obtained from the automatic dependent surveillance–broadcast (ADS-B) system used by the aircraft. The ADS-B system combined the GPS position of the aircraft with the flight speed, altitude, heading, and other information. This information was then sent to other aircraft equipped with the ADS-B system and to air traffic control. One of the ADS-B-derived flight paths of a Boeing 737 during landing at Rotterdam–The Hague Airport is shown in Fig. 8.

Fig. 6 Test setup at Rotterdam–The Hague Airport.

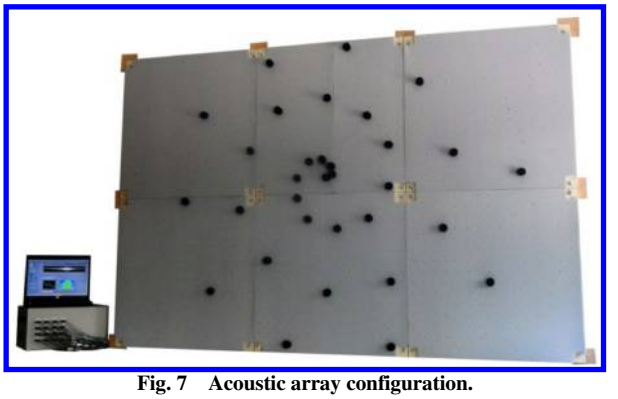

Fig. 7 Acoustic array configuration.

Fig. 5 Position of the acoustic camera with respect to the runway, as indicated by the arrow.

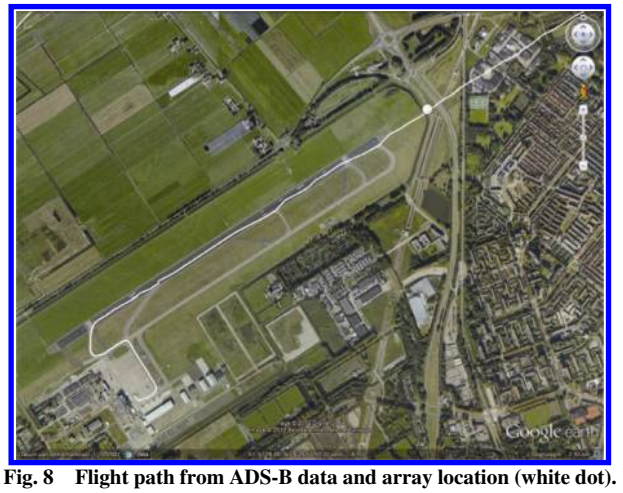

Fig. 8 Flight path from ADS-B data and array location (white dot).

III. Analysis of Acoustic Array Measurements

For each microphone, the 20 ms sound blocks were (fast) Fourier transformed. The 20 ms blocks contained 2000 samples (sampling frequency of 100 kHz), resulting in a 50 Hz frequency resolution in the spectrograms. Per 20 ms block, no weighting nor spectral averaging was applied. Figure 9 presents the spectrogram for one of the flyover measurements obtained when combining all blocks. We used the spectrograms for synchronizing the acoustic data with the ADS-B data and for determining the aircraft engine settings; see Sec. III.A. Next, the measurements of all microphones were combined for beamforming in order to be able to assess the contributions of the individual noise sources. The applied beamforming method is outlined in Sec. III.B, whereas the beamformed data are presented in Sec. III.C.

A. Determination of Engine Fan Settings from the Spectrogram

In Fig. 9, the spectrogram of one of the measurements can be seen. In this figure, Doppler-shifted tones due to the fan rotation can clearly be observed. To retrieve the frequency emitted by the source corresponding to these lines, first, the theoretical Doppler-shifted frequencies are calculated using

$$\frac{f'}{f} = \frac{c}{c + \mathrm{d}r/\mathrm{d}t} \tag{1}$$

in which f' is the observed frequency, f is the source frequency, c is the speed of sound, and $\mathrm{d}r/\mathrm{d}t$ is the rate of change of the distance between the microphone and the source, which is given by

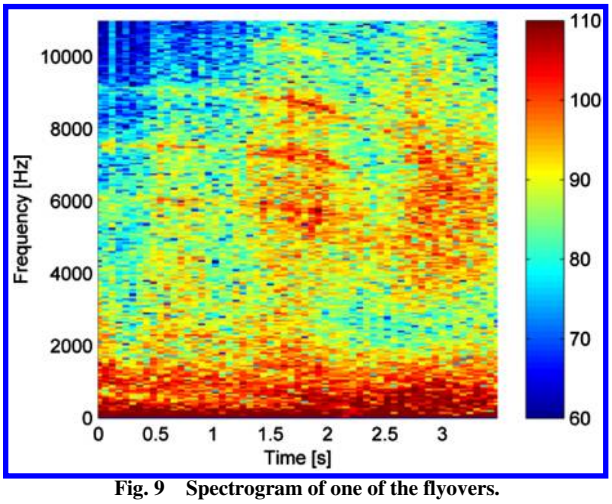

Fig. 9 Spectrogram of one of the flyovers.

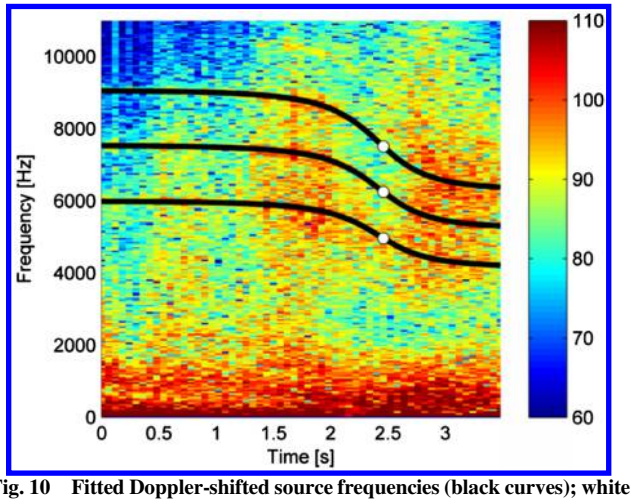

Fig. 10 Fitted Doppler-shifted source frequencies (black curves); white circles indicate time at which aircraft was closest to the array.

Table 1 Harmonics f_3 to f_7 observed from the spectrograms

Measurement	f_3, Hz	f_4, Hz	f_5, Hz	f_6, Hz	f_7, Hz
1	— —	4920	6190	7440	— —
2	— —	— —	5400	6910	8210
4	— —	4370	5420	6530	7650
8	3450	4660	5860	6980	— —
14	3740	5050	6300	7560	— —
18	— —	4450	5590	6790	— —
19	— —	4210	5220	6360	7780
20	— —	5150	6430	7700	8940

Table 2 f_1, fan RPM, and the percentage of maximum

Measurement	f_1, Hz	Fan RPM	Fan RPM, %
1	1237	3093	59.8
2	1145	2862	55.3
4	1090	2724	52.7
8	1165	2912	56.3
14	1259	3148	60.8
18	1123	2808	54.3
19	1076	2690	52.0
20	1282	3205	62.0

$$\frac{\mathrm{d}r}{\mathrm{d}t} = \frac{\boldsymbol{v} \cdot \boldsymbol{r}}{\|\boldsymbol{r}\|} \tag{2}$$

where $\boldsymbol{v}$ is the velocity of the source, and $\boldsymbol{r}$ is the vector from a microphone to the source. The velocity and position vectors are both known from the ADS-B data. Using this, the theoretical Doppler-shifted frequency function [Eq. (1)] is calculated and plotted on top of the spectrogram. By varying the source frequency f, the theoretical line can be optimally matched to the measured line, as shown in Fig. 10.

It is observed that the obtained frequency increments for the three lines shown are virtually constant, and are hence harmonics of each other. Table 1 presents the frequencies of the fan blade passing frequency harmonics observed in the spectrograms. Harmonics 4, 5, and 6 are visible for the majority of the flyovers, whereas harmonics 3 and 7 are sometimes visible. The numbering of the observed harmonics is deduced as follows:

We assume that the observed harmonics are integer multiples of f_1, which is the blade passage frequency of the fan. Hence, we assume that f_1 can be determined from the observed harmonics by fitting a linear function to the harmonics of Table 1 using the least-squares approach.

Figure 11 shows the data of Table 1 (indicated by the stars), the linear fit as a solid line, and the resulting f_1 (indicated by the open circle). Table 2 presents the estimates for f_1.

Subsequently, the rotational speed of the fan is calculated from f_1 using

$$n = \frac{60 f_1}{B} \tag{3}$$

Here, B is the number of blades on the engine fan (24 in this case) and n is the number of rotations per minute (RPM) of the fan. Finally, the fan RPM percentage is calculated using $\mathrm{RPM}_{\max} = 5380$ (corresponding to 104%). For the eight flyovers considered in this study, the found RPM percentages vary between 52 and 62%; see Table 2. These numbers are used in a later stage when a correlation is made with the observed aircraft noise levels on the ground (see Sec. IV).

From this analysis, it has now also become known in which sound block the aircraft is closest to the acoustic array, since in this block, the source frequency is observed. From here on, this block shall be

Downloaded by TU DELFT on February 15, 2018 | http://arc.aiaa.org | DOI: 10.2514/1.C033020

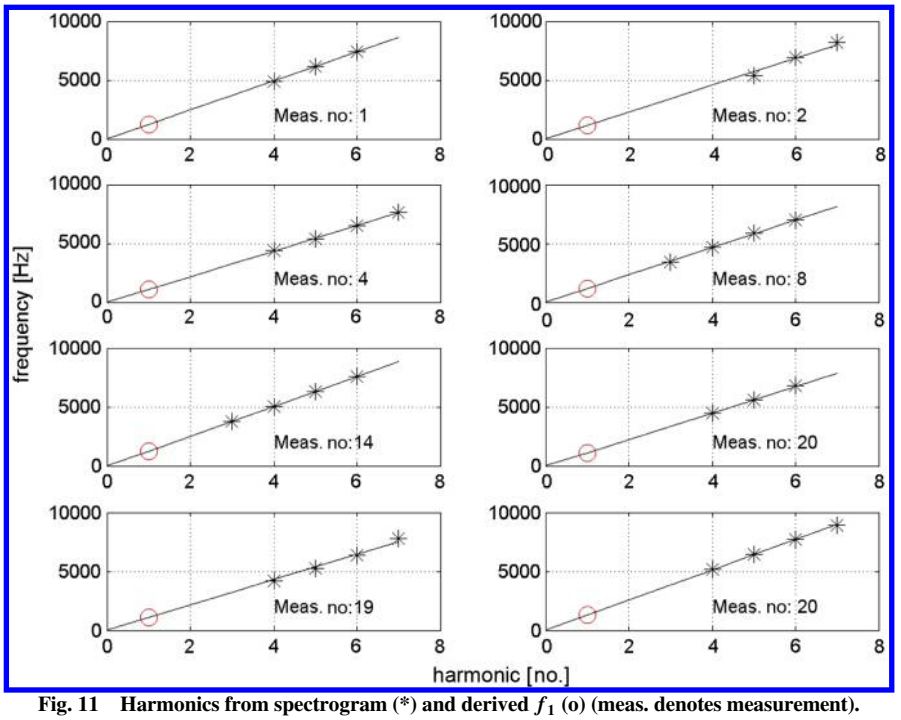

Fig. 11 Harmonics from spectrogram (*) and derived f_1 (o) (meas. denotes measurement).

Downloaded by TU DELFT on February 15, 2018 | http://arc.aiaa.org | DOI: 10.2514/1.C033020

called block 0. Blocks before in time are numbered in the negative, and blocks later in time are numbered in the positive.

One other important aspect of fitting the theoretical Doppler line to the data is the time synchronization between the acoustic data and the ADS-B data, as the data acquisition system of the acoustic camera and the ADS-B transponder both use their own clock. Unfortunately, these clocks are not synchronized, so this has to be done afterward.

B. Applied Beamforming Method

Beamforming can be applied in the time domain and frequency domain. Frequency domain beamforming is computationally very efficient and allows for beamforming (i.e., imaging the noise sources) at selected frequencies. We therefore apply conventional beamforming in the frequency domain and, as is often done, a monopole source model is used to describe the sound pressure field [17]. For microphone m, the acoustic pressure at the microphone p_m and the pressure p_0 at a reference distance r_0 from the source are related by

$$p_0(t) = \frac{r_m}{r_0} p_m(t + \Delta t_m) \tag{4}$$

in which r_m is the distance from the source to the microphone m accounting for the spherical spreading of the sound, and Δt_m is the time it takes for the sound to get from the source to the microphone. The Fourier transform of this equation is given by

$$P_0(f) = \frac{r_m}{r_0} P_m(f) e^{2\pi i f \Delta t_m} \tag{5}$$

which is implemented in practice as a discrete fast Fourier transform.

To find a solution for the complex amplitude $P_0(f)$, we proceed as follows: First, Eq. (5) is rewritten as

$$P_m(f) = P_0(f) \frac{r_0}{r_m} e^{-2\pi i f \Delta t_m} \tag{6}$$

The transfer functions from the source to the microphone (at each frequency) are put into the steering vector $\boldsymbol{g}$, the components of which are

$$g_m(f) = \frac{r_0}{r_m} e^{-2\pi i f \Delta t_m} \tag{7}$$

After Fourier transforming the acoustic data, the resulting Fourier coefficients $P_m(f)$ are put into the vector $\boldsymbol{P}$. An estimate for the acoustic pressure amplitude $P_0(f)$ at this frequency at the reference distance can now be obtained by minimizing the function

$$J = \|\boldsymbol{P} - P_0(f)\boldsymbol{g}\| \tag{8}$$

in a least-squares sense. The solution of this is

$$\hat{P}_0(f) = \frac{\boldsymbol{g}^* \boldsymbol{P}}{\|\boldsymbol{g}\|^2} \tag{9}$$

in which * denotes the complex conjugate transpose of the vector, and $\hat{P}_0(f)$ denotes the least-squares solution for the complex amplitude at the reference distance.

Sound pressure levels are computed from effective pressures. The effective or root-mean-square pressure of a sinusoidal sound wave with frequency f is given by $p_e = |\hat{P}_0(f)|/\sqrt{2}$. With this, the source autopowers for one frequency are defined as

$$A = p_e^2 = \frac{1}{2}|\hat{P}_0(f)|^2 = \frac{1}{2}\hat{P}_0(f)\hat{P}_0^*(f) \tag{10}$$

Substitution of Eq. (9) in Eq. (10) yields

$$A = \frac{1}{2}\frac{\boldsymbol{g}^* \boldsymbol{P}}{\|\boldsymbol{g}\|^2}\left(\frac{\boldsymbol{g}^* \boldsymbol{P}}{\|\boldsymbol{g}\|^2}\right)^* = \frac{1}{2}\frac{\boldsymbol{g}^* \boldsymbol{P}\boldsymbol{P}^* \boldsymbol{g}}{\|\boldsymbol{g}\|^4} \tag{11}$$

This equation is known as "conventional beamforming," where A is a function of f. Since, in general, not only the source strength is unknown but also the source location, Eq. (11) is evaluated for a large range of possible source locations, i.e., grid points with coordinates $\boldsymbol{\xi}_j$ with steering vector components

$$g_m(f, \boldsymbol{\xi}_j) = \frac{r_0}{r_{m,j}} e^{-2\pi i f \Delta t_{m,j}} \tag{12}$$

where Δt_m and r_m have now become dependent on grid point j. The quantity A, now a function of $\boldsymbol{\xi}_j$, is known as the source plot or source

map for frequency f. Various source plot results, obtained from the acoustic flyover data, are shown in the next section.

C. Beamformed Results

The beamforming algorithm described in the previous section is applied to the eight selected flyover measurements. The resulting source maps are shown in Fig. 12 for block 0. Beamforming is done for frequencies in the band of 1500–7500 Hz (frequency step 50 Hz). The upper boundary was chosen to include all higher harmonics, which are clear engine tones. The lower boundary excludes low-frequency noise, which would deteriorate the spatial resolution of the source map (spatial resolution of classical beamforming being inversely proportional to frequency). As an example, illustrating the effects of frequency on beamforming, Fig. 13 shows for measurement 20 the source map for the frequency bands of 1500–1600 and 7100–7200 Hz. Clearly, the resolution for the low frequencies is worse compared to the high frequencies. For the high frequencies, however, the source map shows many side and grating lobes. To counteract these two effects, it is beneficial to use a large range of frequencies, thereby averaging away side and grating lobes that are differently positioned at the various frequencies while at the same time preserving the good resolution at the higher frequencies.

The source maps shown in Fig. 12 are obtained by simply adding (incoherently) the maps obtained at all individual frequencies in the band of 1500–7500 Hz.

To make the source map clearer, the $1/r_m$ scaling in Eq. (7) has been removed: grid points close to the edges of the source maps are further away from the microphones than grid points in the center, and are hence amplified more by applying the spherical spreading correction. Even though the sound pressure levels (SPL) at the edges are relatively low, this correction would amplify them to the same order of magnitude as the actual sound sources. The spherical spreading correction, for clarification, is therefore removed from the images. However, for further analysis (see Sec. IV), the spherical spreading correction should be applied, which can easily be achieved by adding $20 \log 10(r)$ to the values obtained from the images in Fig. 12.

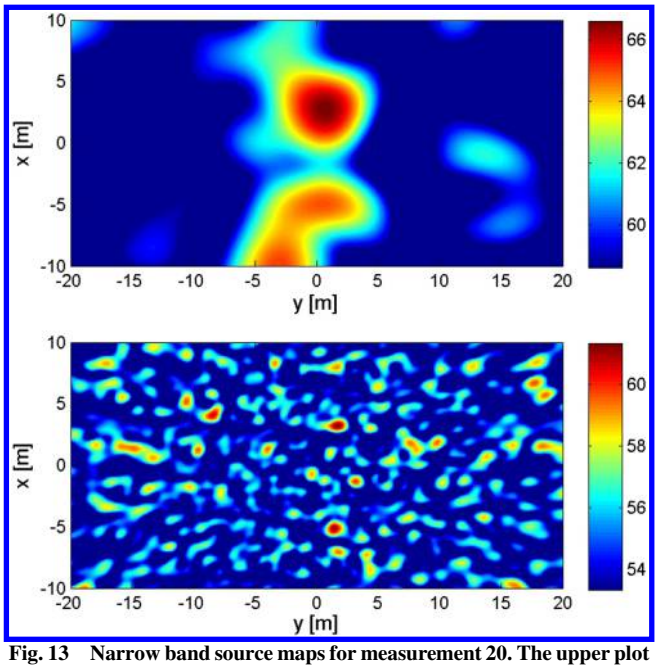

Fig. 13 Narrow band source maps for measurement 20. The upper plot shows the source map for frequencies around 1550 Hz. The lower subplot shows the map for frequencies around 7150 Hz.

The two engines of the aircraft can clearly be seen in all eight source maps. The sources do not appear at the $y = 0$ line, because the

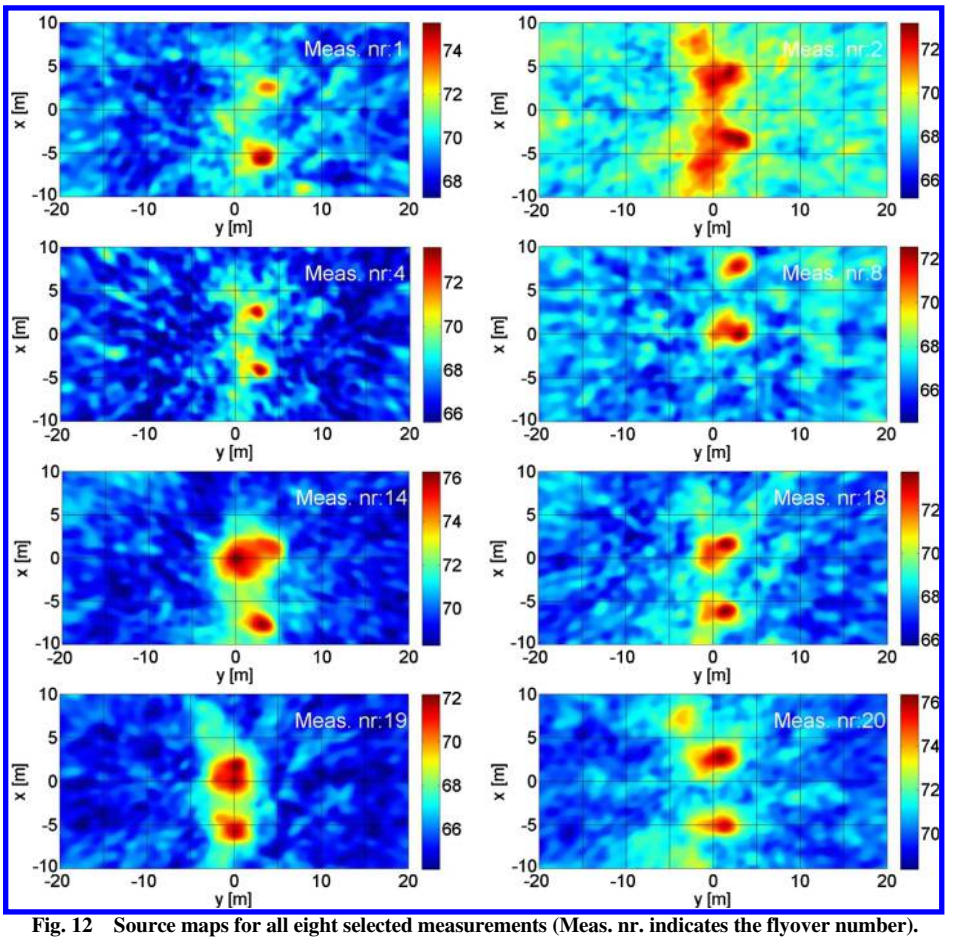

Fig. 12 Source maps for all eight selected measurements (Meas. nr. indicates the flyover number).

Downloaded by TU DELFT on February 15, 2018 | http://arc.aiaa.org | DOI: 10.2514/1.C033020

aircraft are in descent and the line perpendicular to the flight path is hence at a small angle with respect to the vertical. Also, there is a slight variation in flight phase between the blocks because of the 40 ms gaps between the sound blocks.

The SPLs of the individual engines can be read from the source maps of Fig. 12 and used for further analysis (next section).

IV. Results and Discussion of Variability

First, the variability in sound pressure levels for the flyovers is assessed by plotting the overall sound pressure level (OSPL; determined from the pressure time series) against the fan rotational speed (Sec. III.A). The OSPL is calculated for each data block acquired by the separate microphones (i.e., no beamforming applied yet) and corrected for spherical spreading (atmospheric absorption can be neglected, since the distances involved are small). Subsequently, a straight line is fitted through the data points. The results for block 0 can be found in Fig. 14. We also determined the correlation coefficient ρ, the coefficient of determination ρ^2, and the corresponding p value (see Table 3). The whole process is then repeated for all data blocks of interest.

The same procedure is applied to the SPL values for the two engines extracted as peak values from the beamforming images in Fig. 12 (again corrected for spherical spreading). Also, a linear fit is determined and the correlation coefficients and p values are calculated. The results for block 0 are shown in Fig. 15. All correlation coefficients, coefficients of determination, and p values are presented in Table 3 for the left engine, right engine, and overall SPL. Graphical representations of Table 3 can be seen in Figs. 16–18.

The p value is a measure of significance of the found correlation. A p value of, say, 0.05 means that there is a 5% chance that we would obtain that correlation coefficient when, in fact, the variables are unrelated, i.e., uncorrelated. The p value should be low and, typically, a value of 0.05 is used, i.e., the p value should be lower than 5% for the found correlation coefficient to be significant.

The coefficient of determination ρ^2 is the fraction of the variance in the two variables that is shared: e.g., if $\rho = 0.83$ (block 0, left engine), and thus $\rho^2 = 0.69$, then 69% of the total variance observed in SPL of the left engine can be explained by variations in fan rotational speed.

The obtained correlation coefficients are fairly high and, except for data block 2, they are all statistically significant. In addition, it is clearly observed that beamforming substantially increases the correlation between the produced noise levels and the engine fan speed. The reason is the elimination of contributions of other noise sources, both due to the selection of the relevant frequency range and the selection of the relevant spatial area. Also, more than 70% of the observed total variation in the SPLs of the engines can be explained by changes in the corresponding engine settings, i.e., the corresponding fan rotational speeds.

The total noise level variability observed from Figs. 14 and 15 is 6 to 8 dB, depending on whether beamforming is applied or not. As pointed out at the end of Sec. II.A, we may assume the variability due the atmosphere and the source (i.e., the aircraft) to be independent statistical processes. We consider this to be a fair assumption, as variability at the source [e.g., due to changing flight parameters (even if caused by the atmosphere)] should be independent from variability in sound propagation through the atmosphere due to, e.g., turbulence closer to the receiving array. Since the latter is, at most, 2 dB, it can be concluded that the influence of the atmosphere can be neglected and that the observed total noise level variability of 6 to 8 dB is purely due to the source. As mentioned previously, more than 70% of the variations in the noise from the aircraft engines can be explained by the engine setting alone. A possible factor contributing to the remaining 30% is the effect of the changing source directivity, since not all aircraft were exactly overhead of the array.

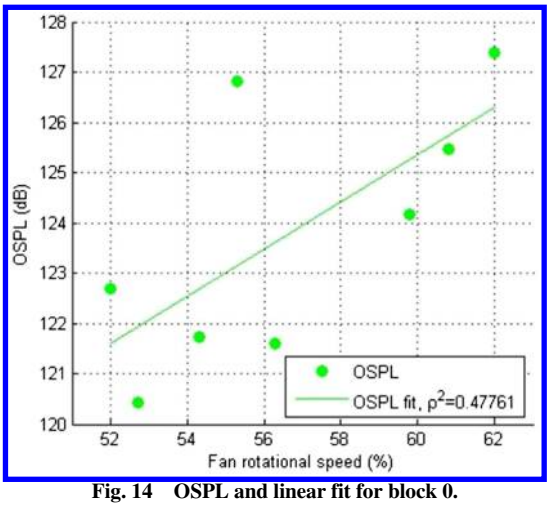

Fig. 14 OSPL and linear fit for block 0.

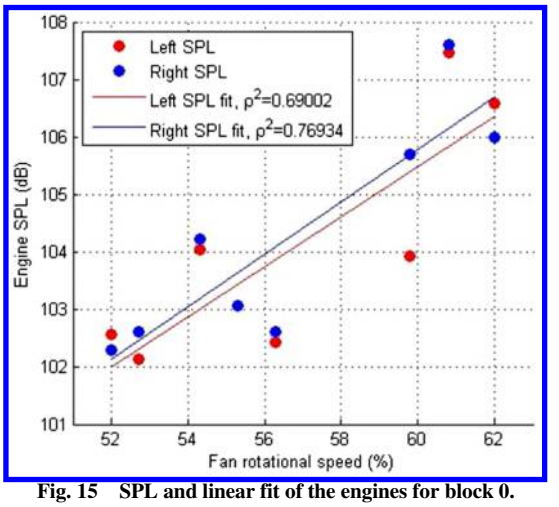

Fig. 15 SPL and linear fit of the engines for block 0.

As mentioned in the Introduction (Sec. I), noise level variations, observed for the same aircraft type, are problematic for noise assessment around airports and the related enforcement of environmental laws. The present research has, however, clearly demonstrated that, for the flight phase considered in this contribution, these noise level variations are mainly due to variations at the source (i.e., the aircraft itself): in our situation, changes in the fan rotational speed of the turbofan engines. To resolve the raised issue in this paper, at least partially, we advise to incorporate the engine setting of the aircraft into models for noise contour calculations around airports with more detail, i.e., based on radar or more precisely modeled flight-path information. For aircraft at larger heights, the effects of variations in the propagation through the atmosphere will become more pronounced. Then, knowing the variability of the aircraft as a noise source is essential for quantifying the contributions of the variable atmosphere.

Table 3 Correlation coefficients, coefficients of determination, and p values

	ρ			ρ^2			p values		
Block	Left	Right	OSPL	Left	Right	OSPL	Left	Right	OSPL
−2	0.6996	0.7163	0.6485	0.4894	0.5131	0.4205	0.0534	0.0456	0.0820
−1	0.7553	0.7993	0.4699	0.5705	0.6389	0.2208	0.0496	0.0310	0.2874
0	0.8307	0.8771	0.6911	0.6900	0.7693	0.4776	0.0106	0.0042	0.0577
1	0.7562	0.6983	0.3654	0.5718	0.4876	0.1335	0.0492	0.0810	0.4202
2	0.6016	0.4087	0.5166	0.3619	0.1670	0.2669	0.1147	0.3148	0.1899

Downloaded by TU DELFT on February 15, 2018 | http://arc.aiaa.org | DOI: 10.2514/1.C033020

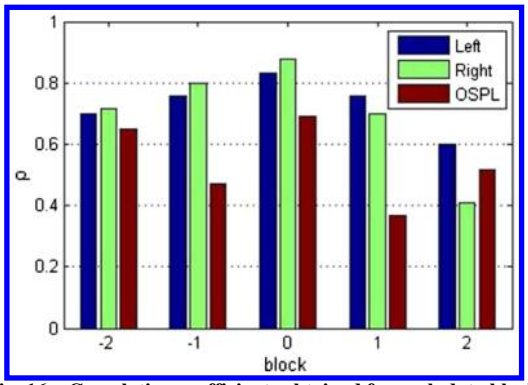

Fig. 16 Correlation coefficients obtained for each data block.

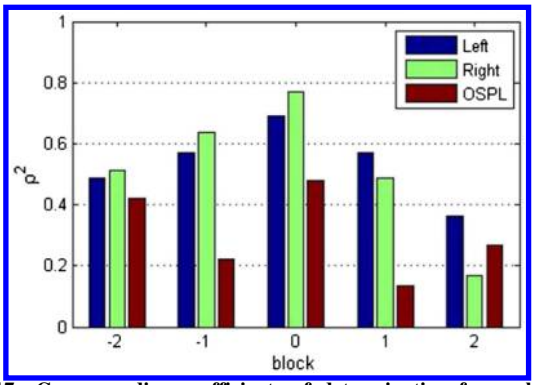

Fig. 17 Corresponding coefficients of determination for each data block.

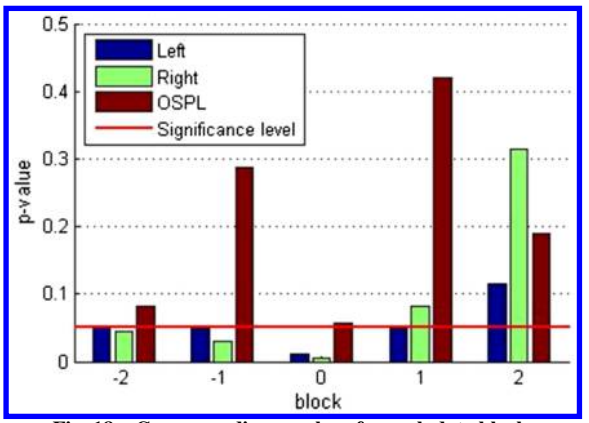

Fig. 18 Corresponding p values for each data block.

V. Conclusions

In this work, the issue of noise level variations as observed for aircraft flyovers directly under the flight path was addressed. This variability, observed for the same aircraft type, can be as large as 12 dB, and hence is problematic for noise assessment around airports and the related enforcement of environmental laws. Noise assessment models that rely on noise–power–distance tables, such as the integrated noise model, do not address this issue, as they provide only averaged (thus fixed) values of actual aircraft noise levels.

It was assumed that the observed noise level variability on the ground was due to the effect of the variable atmosphere (caused, for example, by turbulence) on acoustic propagation and variations in the emitted noise at the source, i.e., the aircraft itself. Both contributions were quantified in dedicated experiments. The atmospheric contribution was determined separately in an experiment where a loudspeaker, mounted at a 100 m height on a meteorological tower, was sending broadband signals to microphones on the ground. The variability in the received sound pressure levels, observed during more than one year, was less than 2 dB and showed no correlation with the weather parameters (like the mean and standard deviation of the windspeed) measured simultaneously.

Noise levels from real aircraft flyovers were measured with an acoustic camera in a second dedicated experiment performed at an airport. The total variability in noise level observed directly under the flight path was 6–8 dB for several landings of the same aircraft type (Boeing 737-700 of the same airline). The imaging capabilities of the acoustic camera allowed for excluding variations due to the ground reflection and ambient noise. The acoustic images obtained revealed the two turbofan engines as the dominant noise sources (in the band of 1500–7500 Hz).

Assuming the noise level variability due to the atmosphere and the source to be independent statistical processes, and knowing that the atmosphere contributes, at most, 2 dB, it can be concluded that the observed total noise level variability (6–8 dB) is entirely due to the source. A correlation analysis showed that the observed noise levels of the engines, as extracted from the acoustic images, are highly related to the fan rotational speed of the turbofan engines. The latter is obtained from the Doppler shift of the fan tones observed in the spectrogram of the data of a single microphone. Statistically significant correlation coefficients higher than 0.8 were obtained, meaning that more than 70% of the observed total variation in engine noise level could be explained by changes in the corresponding engine setting. Hence, to solve at least part of the airport noise assessment problem related to the large noise level variation observed for flyovers of the same aircraft type, it is concluded that it is necessary to incorporate a more accurate engine setting of the aircraft into models for noise contour calculations around airports.

References

[1] "Procedure for the Calculation of Airplane Noise in the Vicinity of Airports," Soc. of Automotive Engineers A-21 Committee on Aircraft Noise, Aerospace Information Rept. AIR 1845, Warrendale, PA Jan. 1986.

[2] "Recommended Method for Computing Noise Contours Around Airports," International Civil Aviation Organization, Circular 205-AN/1/25, Montreal, 1988.

[3] "Report on Standard Method of Computing Noise Contours Around Civil Airports," *European Civil Aviation Conference*, 3rd ed., Vols. 1–2, 2005.

[4] Heppe, G. J. T., "Appendices van de Voorschriften voor de Berekening van de Geluidsbelasting in Lden en Lnight voor Schiphol en in Lden voor de Overige Burgerluchthavens Bedoeld in Artikel 8.1 van de Wet Luchtvaart," National Aerospace Lab./NLR, Rept. NLR-CR-96650-L, Ver. 12.1, Amsterdam, 2011.

[5] He, B., Dinges, E., Hemann, J., Rickel, D., Mirsky, L., Roof, C. J., Boeker, E. R., Gerbi, P. J., and Senzig, D., "Integrated Noise Model (INM) Version 7.0 User's Guide," U.S. Dept. of Transportation, Federal Aviation Administration, Rept. FAA-AEE-07-04, Washington, D.C., April 2007.

[6] Boeker, E. R., Dinges, E., He, B., Fleming, G. G., Roof, C. J., Gerbi, P. J., Rapoza, A. S., and Hemann, J., "Integrated Noise Model (INM) Version 7.0 Technical Manual," U.S. Dept. of Transportation, Federal Aviation Administration, Rept. FAA-AEE-08-01, Washington, D.C., Jan. 2008.

[7] Bergmans, D., Arntzen, M., and Lammen, W., "Noise Attenuation Directly Under the Flight Path," National Aerospace Laboratory/NLR, Rept. NLR-TP-2011-262, Amsterdam, 2011.

[8] "Specifications for Octave-Band and Fractional-Octave-Band Analog and Digital Filters," American National Standards Inst, STD-S1.11-1986, Acoustical Soc. of America STD 65-1986, Washington, D.C., 1993.

[9] Hebly, S., Sindhamani, V., Arntzen, M., Bergmans, B., and Simons, D., "Noise Attenuation Directly Under the Flight Path in Varying Atmospheric Conditions," National Aerospace Lab./NLR Rept. NLR-TP-2013-453, Amsterdam, 2013.

[10] "Standard Values of Atmospheric Absorption as a Function of Temperature and Humidity," Soc. of Automotive Engineers Rept. SAE-ARP-866A, Warrendale, PA, March 1975.

[11] Simons, D., Snellen, M., and Ainslie, M., "A Multivariate Correlate Analysis of High-Frequency Bottom Backvariationing Strength

Downloaded by TU DELFT on February 15, 2018 | http://arc.aiaa.org | DOI: 10.2514/1.C033020

Measurements with Geotechnical Parameters," *Ocean Engineering*, Vol. 32, No. 3, 2007, pp. 640–650.

[12] Deloach, R., "On the Excess Attenuation of Sound in the Atmosphere," NASA, Langley Research Center Rept. NASA-TN-D-7823, 1975.

[13] Khorrami, M. R., Lockard, D. P., Humphreys, W. M., Jr., and Choudari, M. M., "Preliminary Analysis of Acoustic Measurements from the NASA-Gulfstream Airframe Noise Flight Test," *Proceedings of the 14th AIAA/CEAS Aeroacoustics Conference*, AIAA Paper 2008-2814, 2008.

[14] Barsikow, B., "Experiences with Various Configurations of Microphone Arrays Used to Locate Sound Sources on Railway Trains Operated by the DB AG," *Journal of Sound and Vibration*, Vol. 193, No. 1, 1996, pp. 283–293. doi:10.1006/jsvi.1996.0269

[15] Ostertag, J. S. D., Guidati, S., Guidati, G., Wagner, S., Wilde, A., and Kalitzin, N., "Prediction and Measurement of Airframe Noise on a Generic Body," *6th AIAA/CEAS Aeroacoustics Conference and Exhibit*, AIAA Paper 2000-2063, June 2000.

[16] Dougherty, R. P., and Stoker, R. W., "Sidelobe Suppression for Phased Array Aeroacoustic Measurements," *4th AIAA/CEAS Aeroacoustics Conference*, AIAA Paper 1998-2242, June 1998.

[17] Sijtsma, P., "Phased Array Beamforming Applied to Wind Tunnel and Fly-Over Tests," National Aerospace Lab./NLR Rept. NLR-TP-2010-549, Amsterdam, 2010.

[18] Siller, H. A., "Localisation of Sound Sources on Aircraft in Flight," *Berlin Beamforming Conference*, BeBeC-2012-01, Berlin, Feb. 2012, http://www.bebec.eu/Downloads/BeBeC2012/Papers/BeBeC-2012-01.pdf.

Downloaded by TU DELFT on February 15, 2018 | http://arc.aiaa.org | DOI: 10.2514/1.C033020

This article has been cited by:

1. Ana Vieira, Mirjam Snellen, Dick G. Simons. 2018. Assessing the shielding of engine noise by the wings for current aircraft using model predictions and measurements. *The Journal of the Acoustical Society of America* **143**:1, 388-398. [Crossref]
2. Mirjam Snellen, Roberto Merino-Martínez, Dick G. Simons. 2017. Assessment of Noise Variability of Landing Aircraft Using Phased Microphone Array. *Journal of Aircraft* **54**:6, 2173-2183. [Abstract] [Full Text] [PDF] [PDF Plus]
3. C. Zellmann, B. Schäffer, J. M. Wunderli, U. Isermann, C. O. Paschereit. Aircraft Noise Emission Model Accounting for Aircraft Flight Parameters. *Journal of Aircraft*, ahead of print1-15. [Abstract] [Full Text] [PDF] [PDF Plus]
4. Roberto Merino Martinez, Eleonora Neri, Mirjam Snellen, John Kennedy, Dick Simons, Gareth J. Bennett. Comparing flyover noise measurements to full-scale nose landing gear wind tunnel experiments for regional aircraft . [Citation] [PDF] [PDF Plus]
5. Roberto Merino-Martínez, Mirjam Snellen, Dick G. Simons. 2016. Functional Beamforming Applied to Imaging of Flyover Noise on Landing Aircraft. *Journal of Aircraft* **53**:6, 1830-1843. [Abstract] [Full Text] [PDF] [PDF Plus]
6. Ryan L Harne, Danielle T Lynd. 2016. Origami acoustics: using principles of folding structural acoustics for simple and large focusing of sound energy. *Smart Materials and Structures* **25**:8, 085031. [Crossref]
7. Roberto Merino-Martinez, Lothar Bertsch, Dick G. Simons, Mirjam Snellen. Analysis of landing gear noise during approach . [Citation] [PDF] [PDF Plus]

Downloaded by TU DELFT on February 15, 2018 | http://arc.aiaa.org | DOI: 10.2514/1.C033020